

Contents lists available at ScienceDirect

Measurement

journal homepage: www.elsevier.com/locate/measurement





Schemes of local fitting for damage detection of bars using longitudinal operating deflection shapes measured by 3D laser scanning

Wei Xu^a, Ruiqi Li^a, Weidong Zhu^{b,*}

- ^a Department of Engineering Mechanics, Hohai University, Nanjing 210098, People's Republic of China
- b Department of Mechanical Engineering, University of Maryland, Baltimore County, Baltimore, MD 21250, United States

ARTICLE INFO

Keywords: Damage detection Bar Longitudinal vibration Slope of operating deflection shape 3D laser scanning

ABSTRACT

Longitudinal operating deflection shapes (ODSs) of a bar can be measured by three-dimensional laser scanning. The difference between slopes of ODSs (SODSs) under damaged and intact statuses of the bar can be used to indicate and locate the damage. This study inspects ODSs in a multiscale manner, whereby multiscale ODSs (MODSs) and multiscale SODSs (MSODSs) are produced. Noise interference can be eliminated by increasing scale parameters to their satisfying values. In addition, two schemes of local fitting are applied to measured MODSs to generate locally fitted MSODSs under virtual intact statuses of the bars. By relying on differences between measured and locally fitted MSODSs, two individual damage indices (DIs) are established, namely the type-I DI and the type-II DI, in which damage-induced peaks can indicate and locate the damage. The capability of the two schemes of local fitting is theoretically verified and experimentally validated by detecting two-sided notches in bars.

1. Introduction

Damage detection of bars, based on their longitudinal operating deflection shapes (ODSs) under harmonic excitations, has garnered increased attention in recent years [1–3]. In comparison to various methods for detecting damage in beams using flexural ODSs, measuring longitudinal ODSs poses a greater challenge. For instance, with the advanced non-contact laser scanning measurement technique, obtaining flexural ODSs of a beam only requires a one-dimensional (1D) scanning laser vibrometer (1D-SLV) with a single laser head. However, to measure three-dimensional (3D) motions of a bar and extract longitudinal ODSs, a 3D-SLV equipped with three laser heads is necessary. This enables extraction of longitudinal ODSs from 3D steady-state vibration responses at all measurement points along the length of the bar.

In the context of damage in a beam with reduced cross-sectional dimensions such as a notch, in the aspect of physical sense, it reduces the local bending stiffness of the beam, leading to discontinuities in the second-order derivatives of its flexural ODSs. Building upon this theory, the well-established curvature method was initially introduced by Pandey et al. [4] and further developed over subsequent three decades [5–14]. Similarly, when dealing with a bar exhibiting local damage leading to a reduction in its local axial stiffness, discontinuities in the

first-order derivatives of longitudinal ODSs can be employed for damage detection of the bar [1–3]. This approach mirrors the concept of using curvatures of flexural ODSs. Consequently, curvatures of ODSs (CODSs) and slopes of ODSs (SODSs) contain damage features in a beam/bar subjected to transverse and axial vibrations, respectively. The difference between CODSs/SODSs under damaged and intact statuses of the beam/bar can be utilized to indicate and locate the damage.

Nonetheless, damage detection using CODSs/SODSs faces two significant challenges. First, the presence of noise components in a measured ODS can result in substantial interference, potentially masking the discontinuities caused by damage. Second, ODSs of a beam/bar under its undamaged status are often unavailable for real-world structures. To overcome these challenges, a plethora of methods for damage detection of beams/bars have been developed over the past two decades. These methods are designed to be robust against noise interference and operate independently of baseline ODSs in intact conditions. To mitigate noise interference in CODSs and SODSs, the wavelet transform has been employed for denoising measured ODSs [15–18]. More recently, this technique has been integrated into CODSs [7,11,12] and SODSs [1,2]. Introducing scale parameters into CODSs and SODSs enables a gradual elimination of noise interference as the scale increases, while preserving damage-induced discontinuities for effective damage detection.

E-mail address: wzhu@umbc.edu (W. Zhu).

^{*} Corresponding author.

Specifically, for a bar with local damage, two peaks in wavelettransformed SODSs can be used to localize damage edges [1]. It is noteworthy that when the structure undergoes transverse vibration as a beam, wavelet-transformed CODSs can also be utilized to localize damage edges [2]. Recently, Fourier spectral-based CODSs were proposed, demonstrating an ability to suppress noise [14]. In the realm of reconstructing CODSs of a beam under its virtual intact status, global fitting has been applied either to measured ODSs [12] or to their CODSs [8,9]. However, the absence of baseline CODSs of intact beams poses a challenge for damage detection of real-world structures. Besides the fitting methods mentioned above, other baseline-free approaches have been proposed, which are capable of extracting damage-induced discontinuities in CODSs and SODSs for damage detection of beams and bars, respectively. By selecting appropriate mother wavelets, such as Gaussian wavelets with different orders, vanishing moments of wavelets can make low-order global polynomials in CODSs and SODSs vanish. Consequently, only damage-induced discontinuities that resemble local polynomials of higher orders are retained [17]. From a perspective of energy, the Teager-Kaiser energy of flexural ODSs or CODSs represents point-wise energy for each element of a beam. Slight damage-induced discontinuities in a CODS can be significantly amplified, facilitating easy detection of damage [11]. The Teager-Kaiser energy of a flexural ODS can abruptly change at damage locations while remain constant at intact locations, except near boundaries of the beam [19]. Starting from the equation of motion of a beam element, the concept of the transverse pseudo-force was proposed, treating the damage-induced perturbation to the transverse equilibrium as a virtual force applied to the damage location in the transverse direction. This transverse pseudo-force solely generated by the damage vanishes at intact locations [20–27]. Recently, a similar concept of the axial pseudo-force was formulated from the axial equation of motion of a bar with local damage, offering a means to detect damage by localizing damage edges [3].

It is widely recognized that local damage can cause changes in bending stiffness and/or mass in beam and plate structures, with alterations in natural frequencies often employed for damage detection. However, this criterion is not applicable to a damaged bar, such as one with a notch or crack, as its natural frequencies remain unaffected by the damage, and are solely determined by its length, Young's modulus, and density. In such cases, ODSs of the bar offer advantages over natural frequencies since damage can induce discontinuities at damage edges, allowing for indication and localization of the damage. While numerous studies have focused on extracting damage-induced discontinuities of CODSs/SODSs for damage detection of beams/bars, the majority has concentrated on flexural ODSs of beams, with less attention given to longitudinal ODSs of bars. It is noteworthy that, despite the greater difficulty in exciting and measuring longitudinal vibration compared to flexural vibration, a longitudinal ODS can be valuable for detecting damage in structures such as cables. This is the case because flexural vibration of a cable is primarily governed by the tension rather than the bending stiffness. Crucially, the challenge of reconstructing SODSs under virtual intact statuses still needs to be addressed. This study proposes two schemes of local fitting using longitudinal ODSs measured through 3D laser scanning, allowing for reconstruction of SODSs under virtual intact statuses to facilitate damage detection of bars. Before implementing these fitting schemes, noise components in measured ODSs must be filtered using denoising methods such as multiscale analysis, whereby noise-robust multiscale ODSs (MODSs) are produced.

The rest of this paper is structured as follows. In Section 2, multiscale analysis is integrated into ODSs to effectively eliminate noise interference. Additionally, two schemes (type-I and type-II) of local fitting are introduced for the purpose of detecting damage in bars. Section 3 provides an analytical verification of these two local fitting schemes by employing analytical longitudinal ODSs of bars with local damage. In Section 4, the applicability of the two local fitting schemes is experimentally validated by detecting a two-sided notch in a bar, whose longitudinal ODSs are measured using a 3D-SLV. Finally, Section 5 presents

some concluding remarks.

2. Schemes of local fitting for damage detection of bars

2.1. Damage-induced discontinuities in SODSs

An axial force F(x,t) in a bar can be expressed as [28]

$$F(x,t) = E(x)A(x)\frac{\partial u(x,t)}{\partial x},$$
(1)

where u(x,t) is the longitudinal displacement and A(x) is the cross-sectional area of the bar, with x denoting the abscissa along the bar length and t denoting time. The continuity condition of the axial force at a position $x=x_0$ can be written as

$$E(x)A(x)\frac{\partial u(x,t)}{\partial x}\bigg|_{x=x_0^-} = E(x)A(x)\frac{\partial u(x,t)}{\partial x}\bigg|_{x=x_0^+}.$$
 (2)

The time derivative of Eq. (2) is as follows:

$$E(x)A(x)\frac{\partial v_x(x,t)}{\partial x}\bigg|_{x=x_0^-} = E(x)A(x)\frac{\partial v_x(x,t)}{\partial x}\bigg|_{x=x_0^+},$$
(3)

where $v_r(x,t)$ denotes the longitudinal velocity of the bar.

When the bar is subjected to a single-tone harmonic force, its 3D components of steady-state velocities v_1 , v_2 , and v_3 at each measurement point can be measured using a 3D-SLV, as illustrated in the schematic in Fig. 1. Note that #1, #2, and #3 laser heads of the 3D-SLV measure v_1 , v_2 , and v_3 in the directions of three incident laser beams, respectively. The longitudinal velocity v_x and transverse velocities v_y and v_z can be obtained through the geometrical transformation [29]:

$$\left\{ \begin{array}{l} v_x \\ v_y \\ v_z \end{array} \right\} = \begin{bmatrix} \cos\alpha_1 & \cos\beta_1 & \cos\gamma_1 \\ \cos\alpha_2 & \cos\beta_2 & \cos\gamma_2 \\ \cos\alpha_3 & \cos\beta_3 & \cos\gamma_3 \end{array} \right] \left\{ \begin{array}{l} v_1 \\ v_2 \\ v_3 \end{array} \right\}, \tag{4}$$

where α_i , β_i , and γ_i (i=1,2,3) are angles between incident laser beams and x-, y-, and z-axes of the coordinate system for each laser head. The coordinates of each measurement point enable the automatic calculation of these angles in the 3D-SLV.

It can be assumed that

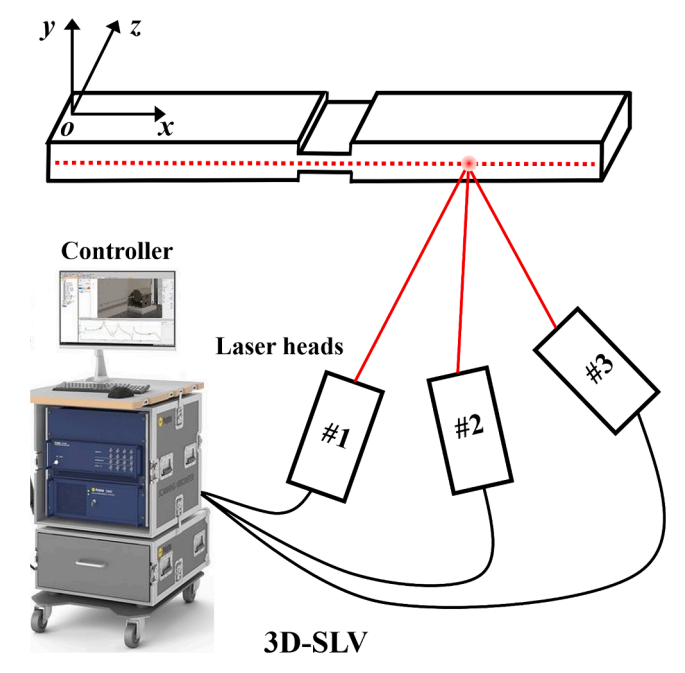


Fig. 1. Schematic of 3D vibration measurement of a bar using a 3D-SLV.

$$u(x,t) = U(x)\sin(\omega t), \tag{5}$$

where U(x) denotes a longitudinal ODS at an excitation frequency ω that is not an undamped longitudinal natural frequency [2,3]. As observed in Fig. 2(a), local damage can barely cause evident changes in a longitudinal ODS of the bar, where superscripts D and I of U(x) denote damaged and intact statuses of the bar, respectively. These two superscripts will continue to be used hereinafter in this study. Therefore, the local damage can be hardly detected directly by the ODS. Without loss of generality, the ODSs in this study are normalized with their absolute maximum being unity. Substituting Eq. (5) into $v_X(x,t) = \frac{du(x,t)}{dt}$ yields

$$v_{x}(x,t) = \omega U(x)\cos(\omega t). \tag{6}$$

Substituting Eq. (6) into Eq. (3) yields

$$E(x)A(x)\frac{dU(x)}{dx}\bigg|_{x=x_0^-} = E(x)A(x)\frac{dU(x)}{dx}\bigg|_{x=x_0^+}.$$
 (7)

By considering a bar with local damage that spans from x_1 to x_2 , Eq. (7) indicates that damage-caused changes in Young's modulus E(x) and/or cross-sectional area A(x) can cause a discontinuity between $x=x_1$ and $x=x_2$ in the SODS $S(x)=\frac{\mathrm{d}U(x)}{\mathrm{d}x}$, as depicted in Fig. 2(b). The physical interpretation of Eq. (7) reveals that the axial force is continuous along the bar regardless of damage. To maintain the balance dictated by Eq. (7), any damage-caused change in E(x)A(x) can lead to a discontinuity in S(x) at the damage location, as indicated by a red circle in Fig. 2(b). Consequently, SODSs can be employed to indicate and locate damage in the bar [1]. It is noteworthy that at locations where SODSs vanish, damage cannot be detected by SODSs because both sides of Eq. (7) are equal to zero regardless of the presence of damage.

However, since noise components are inevitably involved in measured ODSs and can be amplified by differentiation operation [3], actual damage-induced discontinuities in S(x) can be masked by intense noise interference, as illustrated in Fig. 3(a).

By addressing this problem, the measured longitudinal ODSs in this study are inspected in a "region-by-region" manner [3] instead of the conventional "point-by-point" manner: a scaled Gaussian windowing function $\bar{g}_s(x)$ is used to average an ODS, whereby the MODS $U_s(x)$ is produced:

$$\overline{U}(v,s) = \frac{1}{\sqrt{s}} U \otimes \overline{g}_s(v), \tag{8}$$

$$U_s(x) = \overline{U}(v, s)|_{v=x}, \tag{9}$$

where $\bar{g}_s(x)=\frac{1}{\sqrt{s}}g(\frac{-x}{s})$ with the Gaussian function $g(x)=(2/\pi)^{1/4}e^{-x^2}$ and the scale parameter s, and \otimes denotes convolution operation. The Gaussian filter is known for its effectiveness and ease of implementation compared to other filters [30]. It proves useful in significantly reducing noise in an ODS while minimizing loss of damage features [3]. By gradually increasing the scale parameter, noise components in the ODS can be eliminated while the damage-induced discontinuity can be retained [31]. The discrete MSODS $S_s[x_k]$ (see Fig. 3(b)) for the kth measurement point is calculated using the finite difference method [2]:

$$S_s[x_k] = \frac{U_s[x_{k+1}] - U_s[x_{k-1}]}{2h},\tag{10}$$

where k = 2, 3, ..., N-1 with N representing the number of the measurement points and h denoting the spatial sampling interval. As can be seen in Fig. 3(b), noise interference is eliminated in the MSODS and the noise-induced discontinuity arises at damage edges.

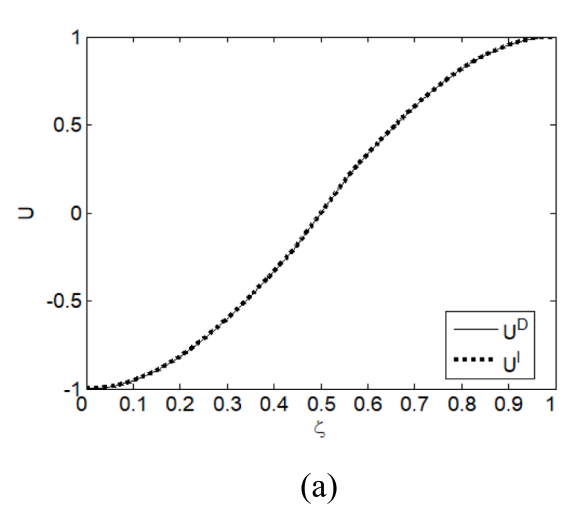
2.2. Type-I and type-II local fitting schemes for damage detection of bars

Two schemes of local fitting are proposed in this study for damage detection of a bar. The common principle of the two schemes of local fitting is to fit the MSODS of the bar under the damaged status through interpolation, which can be regarded as the MSODS of the bar under the virtual intact status. In the aspect of physical sense, the difference between the measured and reconstructed MSODSs represents damage-induced discontinuities at damage edges. The proposed methods enable detection of damage in bars without the need for baseline ODSs in intact conditions, thereby facilitating straightforward operation for real-world structural components.

For the first scheme of local fitting shown in the flowchart in Fig. 4, local cubic interpolation is employed to reconstruct the value of the locally fitted MODS $U_s^{FL}[x_k]$ for the kth measurement point from the measured MODS $U_s^M[x]$:

$$U_s^{F,L}[x_k] = \sum_{r=0}^3 a_{r,k} x^r \bigg|_{x=x_k},$$
(11)

where the coefficients $a_{r,k}$ (r=0,1,2,3) are determined by four neighboring points $(x_{k-2},U_s^M[x_{k-2}])$, $(x_{k-1},U_s^M[x_{k-1}])$, $(x_{k+1},U_s^M[x_{k+1}])$, and $(x_{k+2},U_s^M[x_{k+2}])$ of the curve $U_s^M[x]$. By Eq. (10), the MSODSs $S_s^M[x]$ and $S_{s,l}^{F,L}[x]$ are produced from $U_s^M[x]$ and $U_s^{F,L}[x]$, respectively. Thereby, the type-I DI denoted as $DI_l[x]$ is established, which relies on the difference between $S_s^M[x]$ and $S_{s,l}^{F,L}[x]$:



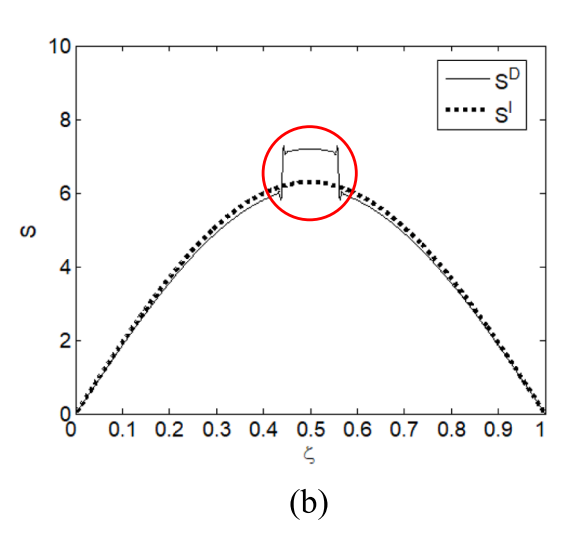


Fig. 2. (a) ODSs and (b) SODSs of a bar under damaged and intact statuses.

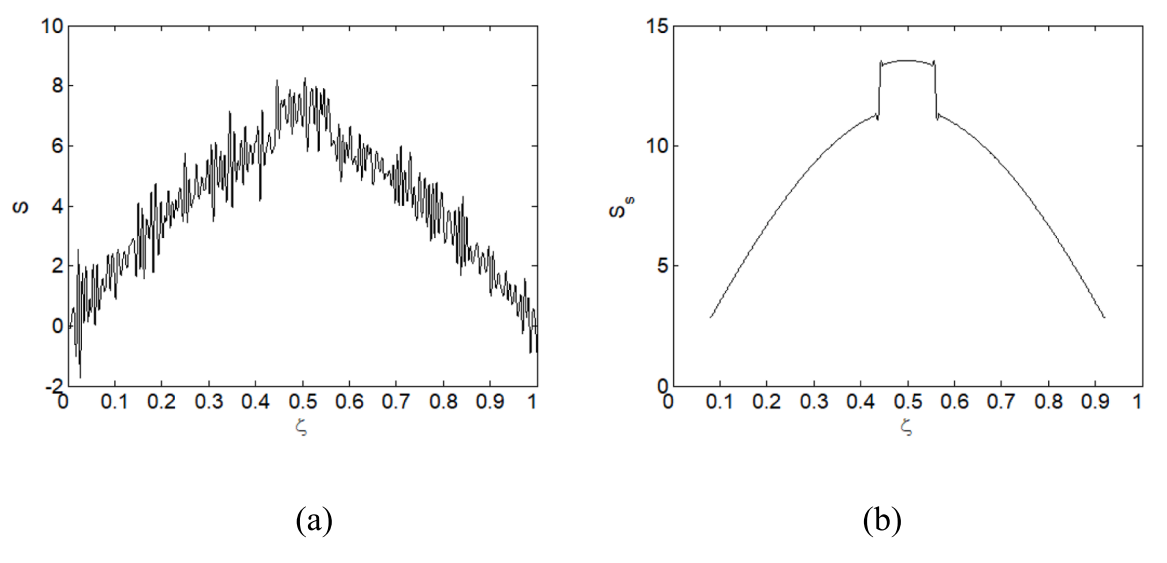


Fig. 3. (a) SODS and (b) MSODS of the damaged bar in a noisy condition.

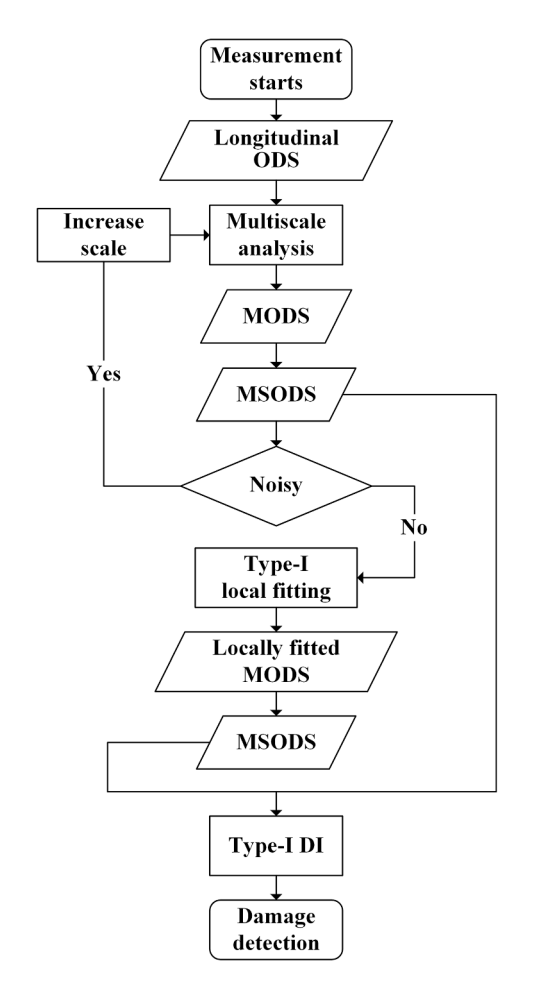


Fig. 4. Flowchart of damage detection of bars using type-I local fitting.

$$DI_{1}[x_{k}] = \frac{\left|S_{s}^{M}[x_{k}] - S_{s1}^{F,L}[x_{k}]\right|}{\max\left|S_{s}^{M}[x_{i}] - S_{s1}^{F,L}[x_{i}]\right|_{i=2,4,5,\dots,N-1}}.$$
(12)

Likewise, the second scheme of local fitting shown in the flowchart in Fig. 5 is proposed by reconstructing the value of the locally fitted MSODS $S_{\rm sll}^{F,L}[x_k]$ for the kth measurement point from the measured MSODS $S_{\rm s}^{g}[x]$ through cubic interpolation for local fitting:

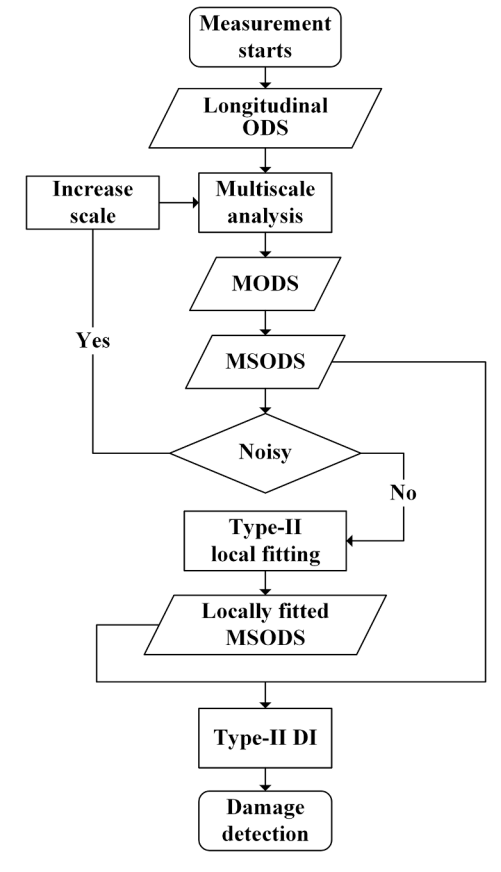


Fig. 5. Flowchart of damage detection of bars using type-II local fitting.

$$S_{\text{sII}}^{F,L}[x_k] = \sum_{r=0}^{3} b_{r,k} x^r \bigg|_{x=x_k}, \tag{13}$$

where the coefficients $b_{r,k}$ (r=0,1,2,3) are determined by four neighboring points $(x_{k-2},S_s^M[x_{k-2}])$, $(x_{k-1},S_s^M[x_{k-1}])$, $(x_{k+1},S_s^M[x_{k+1}])$, and $(x_{k+2},S_s^M[x_{k+2}])$ of the curve $S_s^M[x]$. Similar to the type-I DI, the type-II DI denoted as $DI_{\rm II}[x]$ is established, which relies on the difference between $S_s^M[x]$ and $S_{\rm SII}^{F,L}[x]$:

$$DI_{II}[x_k] = \frac{\left|S_s^M[x_k] - S_{sII}^{F,L}[x_k]\right|}{\max\left|S_s^M[x_i] - S_{sII}^{F,L}[x_i]\right|_{i=2,4,5,...N-1}}.$$
(14)

Note that both types of the aforementioned DIs range from 0 to 1. The locations of the peaks in the DIs can indicate damage edges.

3. Theoretical verification

Analytical solutions to longitudinal ODSs of bars with local damage are employed to theoretically validate the effectiveness of the two proposed schemes of local fitting in this study. Consider a specimen of an aluminum bar with 500 mm in length, 25 mm in width, and 6 mm in thickness, whose Young's modulus is 70 GPa and density is 2700 kg/m^3 .

A two-sided notch with reduced cross-sectional dimensions is modeled by symmetrically reducing the thickness of the specimen by 0.75 mm from both its top and bottom surfaces through its width (as illustrated in Fig. 1). Note that boundary conditions at both ends of the bar are free, with an aim to maintain consistency with the experiment in this study. Without loss of generality, let $\zeta=x/500$ be the dimensionless coordinate. Scenarios I, II, and III are considered with notch locations being [0.4, 0.6], [0.45 0.55], and [0.475 0.525] for ζ , respectively. It is important to note that the longitudinal ODSs of the bars are numerically evaluated using Matlab following the procedure of analytical solutions that can be found in the authors' previous work [2], and the details are not included in this section for the sake of conciseness.

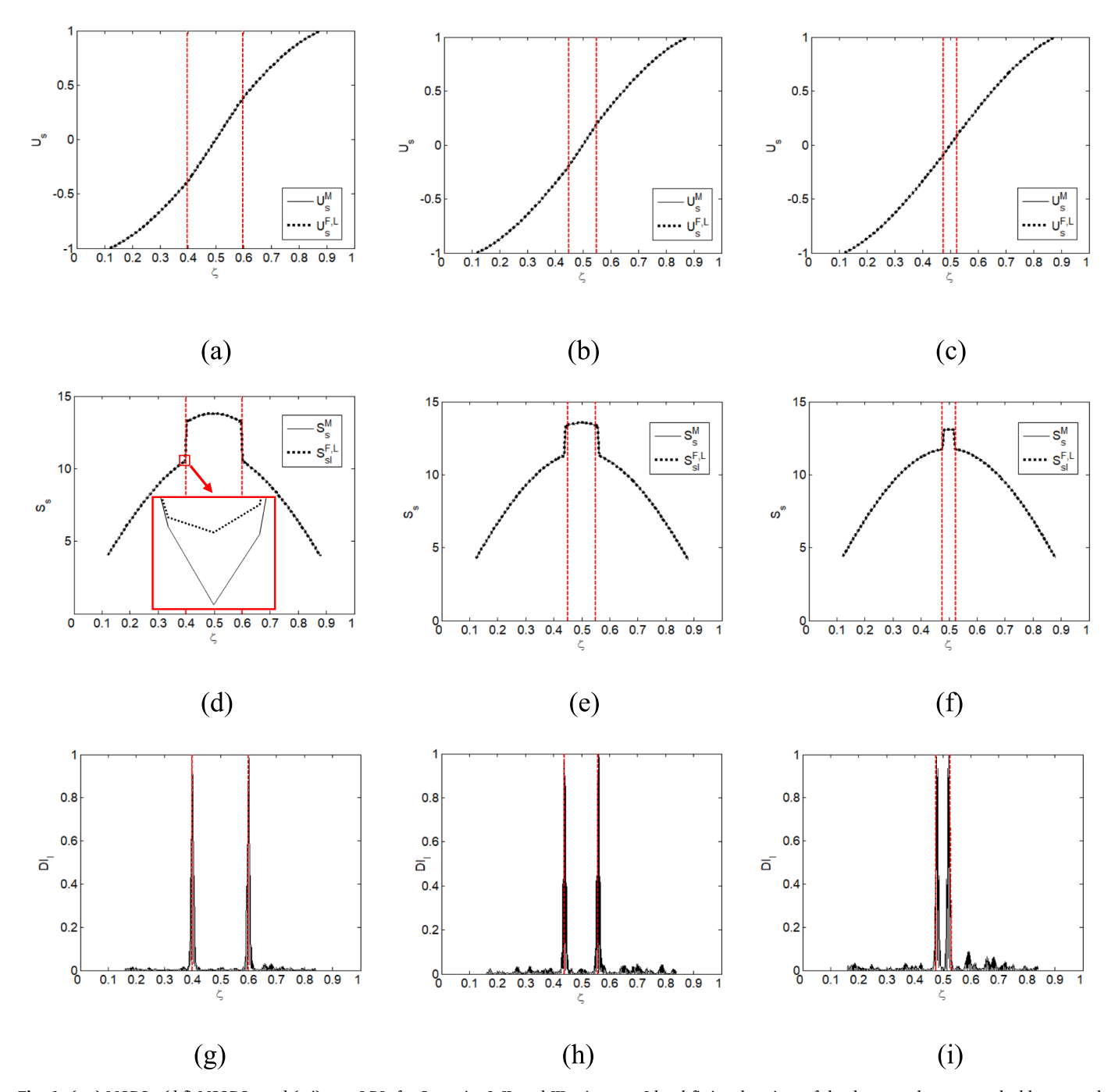


Fig. 6. (a-c) MODSs, (d-f) MSODSs, and (g-i) type-I DIs for Scenarios I, II, and III using type-I local fitting; locations of the damage edges are marked by two red dashed lines. (For interpretation of the references to colour in this figure legend, the reader is referred to the web version of this article.)

3.1. Damage detection by type-I local fitting

In the authors' previous work [3], the ultimate signal-to-noise ratio (SNR) of an analytical longitudinal ODS for damage detection was observed to be 60 dB. With this consideration, the same ultimate noise level is deliberately set by adding white Gaussian noise to the noise-free analytical longitudinal ODSs, resulting in noisy longitudinal ODSs with an SNR of 60 dB. For denoising purposes, measured ODSs for Scenarios I, II, and III are inspected in a "region-by-region" manner by Eqs. (8) and (9), whereby the corresponding MODSs $U_s^M[x]$ at a satisfying scale of 30 are produced, as shown in solid lines in Fig. 6(a), (b), and (c), respectively. According to the theory of multiscale analysis of a signal, the criterion for selecting the optimal scale parameter is as follows: at a smaller scale, noise in MODSs can interfere with MSODSs, potentially masking damage-induced sudden changes in MSODSs, and at a larger scale, edges of those changes may be shifted from actual damage edges [31].

The type-I scheme of local fitting is applied to the measured MODSs $U_s^{M}[x]$ by Eq. (11), resulting in the locally fitted MODSs $U_s^{F,L}[x]$, also shown in dotted lines in Fig. 6(a), (b), and (c). Upon comparison, the curves $U_s^{M}[x]$ and $U_s^{F,L}[x]$ for each scenario are highly identical, demonstrating the validity of the scheme of local fitting. By Eq. (10), the MSODSs $S_s^{M}[x]$ and $S_s^{F,L}[x]$ for Scenarios I, II, and III are obtained from the MODSs $U_s^{M}[x]$ and $U_s^{F,L}[x]$, as shown in Fig. 6(d), (e), and (f), respectively. The curves $S_s^{M}[x]$ and $S_s^{F,L}[x]$ are almost identical except for the details at locations of the damage edges. Low-order global polynomials in measured and locally fitted MSODSs exhibit significant overlap. Conversely, local polynomials of higher orders at the edges of damage-

induced discontinuities cannot be precisely fitted through local cubic fitting. As a result, differences between each pair of the original and fitted curves (refer to Fig. 6(d), for instance) remain at locations of the damage edges, facilitating localization of damage. By relying on the differences between $S_s^M[x]$ and $S_{sI}^{F,L}[x]$, type-I DIs $DI_I[x]$ for Scenarios I, II, and III are obtained by Eq. (12) and shown in Fig. 6(g), (h), and (i), respectively. In each $DI_I[x]$, owing to the differences between $S_s^M[x]$ and $S_{sI}^{F,L}[x]$, two sharply rising peaks evidently indicate the damage location that correspond to actual locations of the damage edges, which are marked by two red dashed lines; meanwhile, each $DI_I[x]$ almost vanishes at intact locations. Therefore, $DI_I[x]$ is an ideal index for indicating and locating damage in bars.

3.2. Damage detection by type-II local fitting

Type-II local fitting is applied to $S_s^M[x]$ by Eq. (13) for Scenarios I, II, and III, as shown in solid lines in Fig. 7(a), (b), and (c), respectively, whereby the corresponding locally fitted MSODSs $S_{sII}^{F,L}[x]$ are obtained and also shown in dotted lines in Fig. 7(a), (b), and (c), respectively. By relying on the differences between $S_s^M[x]$ and $S_{sII}^{F,L}[x]$, type-II DIs $DI_{II}[x]$ for Scenarios I, II, and III are obtained by Eq. (14) and shown in Fig. 7(d), (e), and (f), respectively.

Likewise, the curves $S_s^M[x]$ and $S_{sII}^{F,L}[x]$ are almost identical except for locations of the damage edges. Slight differences between $S_s^M[x]$ and $S_{sII}^{F,L}[x]$ due to fitting-caused smoothing occur at locations of the damage edges, leading to two abrupt peaks in each type-II DI $DI_{II}[x]$ (see Fig. 7 (d)-(f)). The locations of the peaks in $DI_{II}[x]$ are in good agreement with

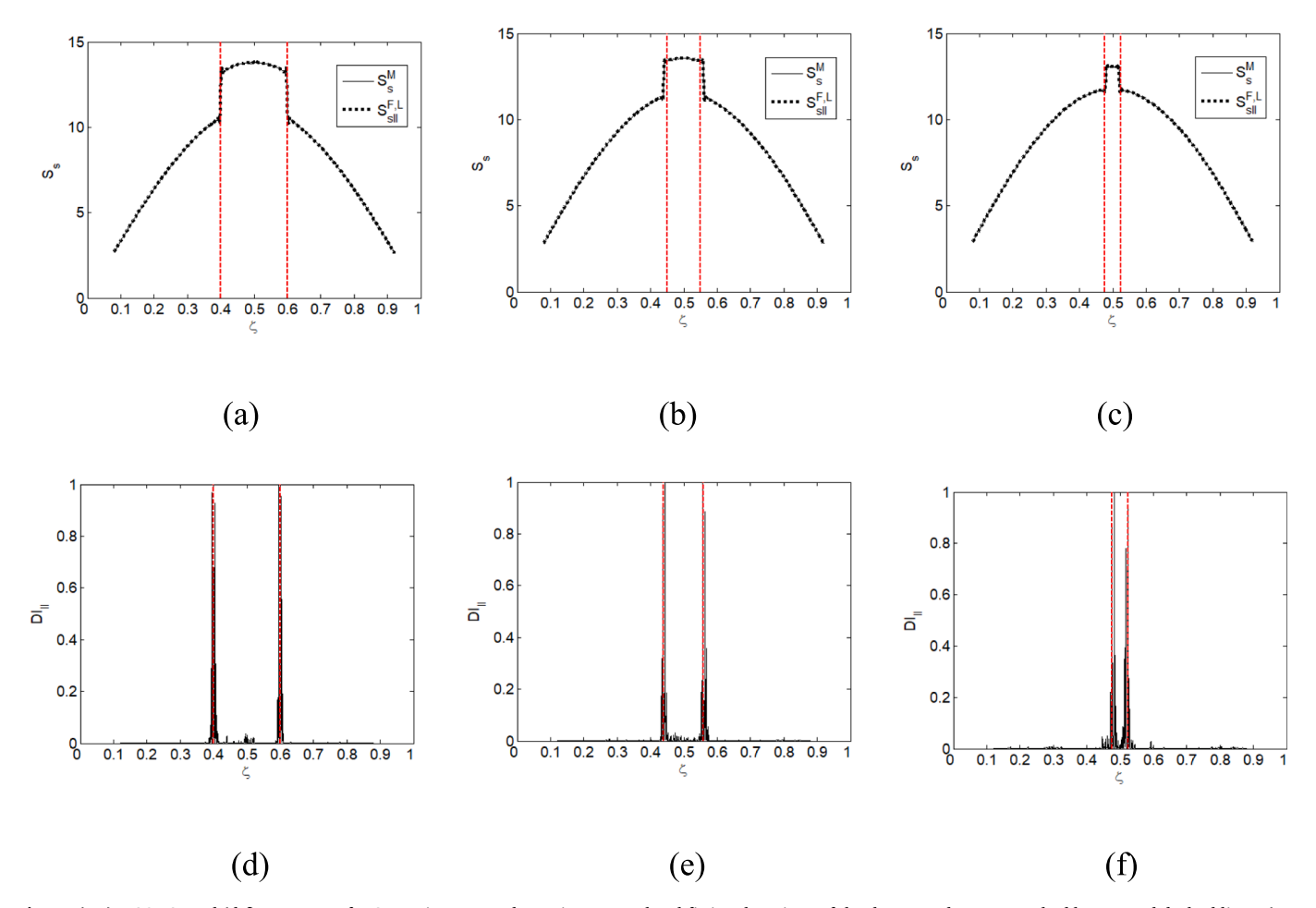


Fig. 7. (a-c) MSODSs and (d-f) type-II DIs for Scenarios I, II, and III using type-II local fitting; locations of the damage edges are marked by two red dashed lines. (For interpretation of the references to colour in this figure legend, the reader is referred to the web version of this article.)

actual locations of the damage edges, which are marked by two red dashed lines. Similar to $DI_{\rm I}[x]$, $DI_{\rm II}[x]$ almost vanishes at intact locations. Therefore, $DI_{\rm II}[x]$ exhibits almost the same capability as $DI_{\rm I}[x]$ for indicating and locating damage in bars.

3.3. Comparison of local and global fitting schemes for damage detection of bars

For comparison purposes, this section employs the existing schemes of global fitting [8,9,12] to reconstruct MSODSs of the bar under the virtual intact status. More specifically, type-I and type-II schemes of

global fitting are introduced.

For type-I global fitting, a global cubic polynomial is used to fit the entire measured MODS $U_s^M[x]$, allowing for reconstruction of the globally fitted MODS $U_s^{F,G}[x_k]$ for the kth measurement point (see Fig. 8(a)-(c)):

$$U_s^{F,G}[x_k] = \sum_{r=0}^{3} c_r x^r \bigg|_{x=x_k},$$
(15)

where the coefficients c_r (r = 0,1,2,3) are determined by all the points of $U_s^M[x]$ using the least-squares method:

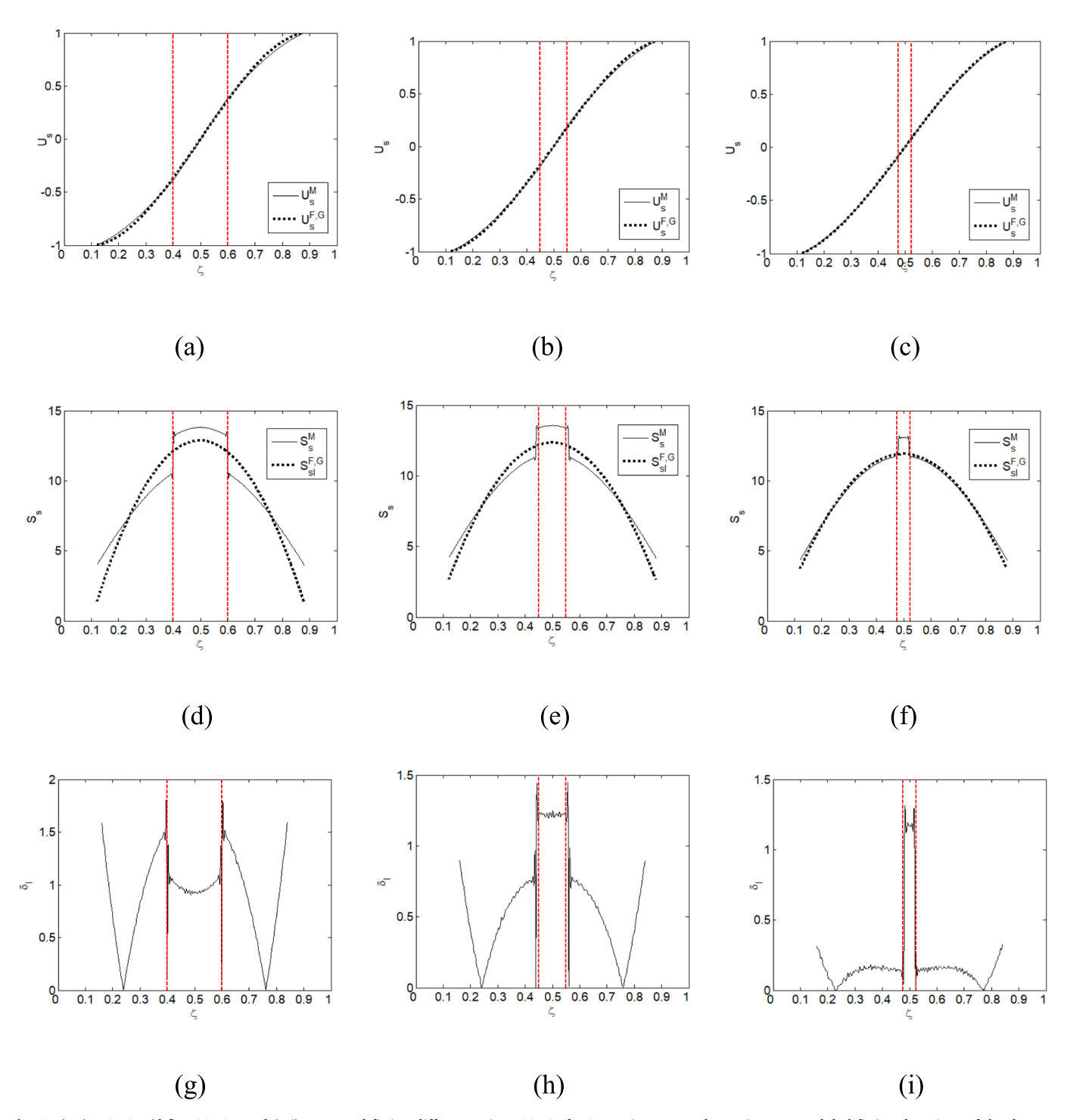


Fig. 8. (a-c) MODSs, (d-f) MSODSs, and (g-i) measured-fitting differences in MSODSs for Scenarios I, II, and III using type-I global fitting; locations of the damage edges are marked by two red dashed lines. (For interpretation of the references to colour in this figure legend, the reader is referred to the web version of this article.)

$$\min \sum_{i=1}^{N} \left(U_s^{M}[x_i] - U_s^{F,G}[x_i] \right)^2.$$
 (16)

On the basis of MODSs $U_s^M[x]$ and $U_s^{F,G}[x]$, the MSODSs $S_s^M[x]$ and $S_{sl}^{F,G}[x]$ are obtained by Eq. (10), respectively (see Fig. 8(d)-(f)). The absolute difference between $S_s^M[x]$ and $S_{sl}^{F,G}[x]$ is denoted as $\delta_l[x]$ (see Fig. 8(g)-(i)):

$$\delta_{I}[x] = |S_{s}^{M}[x] - S_{sI}^{F,G}[x]|. \tag{17}$$

It can be seen from Fig. 8(a)-(c) that differences between $U_s^M[x]$ and $U_s^{F,G}[x]$ increase with damage sizes, yet they are scarcely noticeable. In contrast, the noticeable differences between $S_s^M[x]$ and $S_{si}^{F,G}[x]$ considerably increase, as shown in Fig. 8(d)-(f). It is important to note that when the damage size becomes small enough, the curve $S_{sl}^{F,G}[x]$ approaches $S_s^M[x]$ at intact locations of the bar. In that stituation, type-I global fitting can effectively reconstruct $S_{sl}^{F,G}[x]$ from $S_s^M[x]$, and the major difference between them is localized at the damage location. As exemplified in Fig. 8(i), the peak in $\delta_l[x]$ exhibits a remarkable feature that is suitable for detecting small-sized damage in the bar. Nevertheless, when the damage size increases, the absolute differences $\delta_l[x]$ between $S_s^M[x]$ and $S_{sl}^{F,G}[x]$ (see Fig. 8(g)-(i)) at damage locations become less distinguishable due to the influence of global trends.

For type-II global fitting, a global cubic polynomial is applied to fit the entire measured MSODS $S_s^M[x]$ through global fitting, enabling reconstruction of the MSODS $S_{sII}^{F,G}[x]$ for the kth measurement point (see Fig. 9(a)-(c)):

$$S_{\text{siI}}^{F,G}[x_k] = \sum_{r=0}^{3} d_r x^r \bigg|_{x=0},$$
 (18)

where the least-squares method is also applied to determine the coefficients d_r (r = 0, 1, 2, 3):

$$\min \sum_{i=1}^{N} \left(S_s^M[x_i] - S_{sII}^{F,G}[x_i] \right)^2.$$
 (19)

The absolute difference $\delta_{\rm II}[x]$ (see Fig. 9(d)-(f)) between $S_s^M[x]$ and $S_{s{\rm II}}^{F,G}[x]$ is defined as

$$\delta_{II}[x] = |S_s^M[x] - S_{sII}^{F,G}[x]|. \tag{20}$$

Similar to the situation encountered in type-I global fitting, type-II global fitting reveals increasing differences between $S_s^M[x]$ and $S_{sII}^{F,G}[x]$ with increment of damage sizes (see Fig. 9(a)-(c)). Likewise, as the damage size decreases, the curve $S_{sII}^{F,G}[x]$ converges towards $S_s^M[x]$ at intact locations of the bar, whose primary distinction localizes at the damage location. Consequently, the absolute differences $\delta_{II}[x]$ between $S_s^M[x]$ and $S_{sII}^{F,G}[x]$ at damage locations are obscured by global trends for large-sized damage (see Fig. 9(d) and (e)); in contrast, the difference becomes more pronounced when detecting smaller-sized damage, as exemplified in Fig. 9(f).

In comparison to the performance of damage detection using the schemes of local fitting (see Fig. 6(g)-(i) and Fig. 7(d)-(f)), the schemes of global fitting prove unsuitable for detecting large-sized damage. This limitation arises from deviations at intact locations, as global fitting

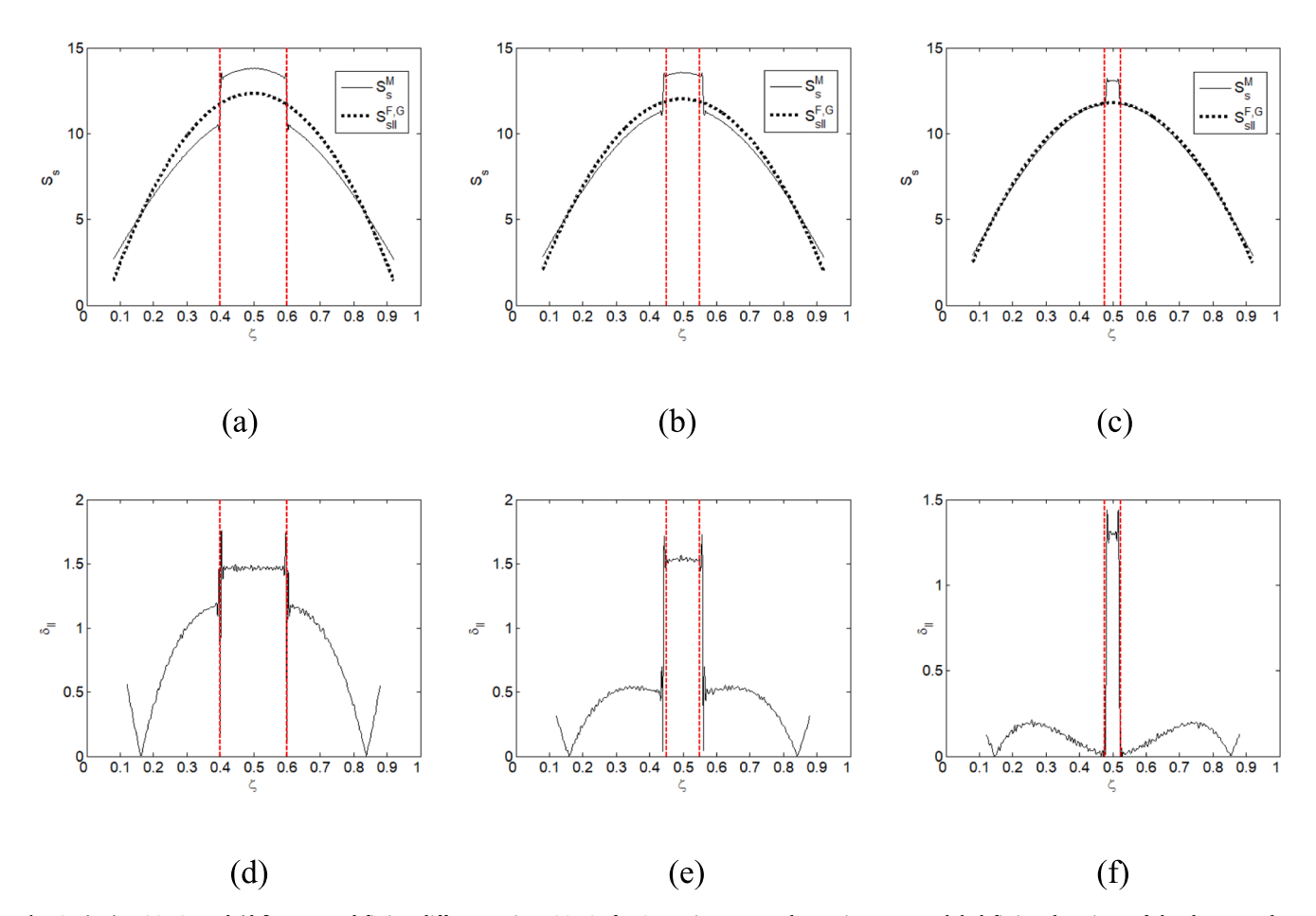


Fig. 9. (a-c) MSODSs and (d-f) measured-fitting differences in MSODSs for Scenarios I, II, and III using type-II global fitting; locations of the damage edges are marked by two red dashed lines. (For interpretation of the references to colour in this figure legend, the reader is referred to the web version of this article.)

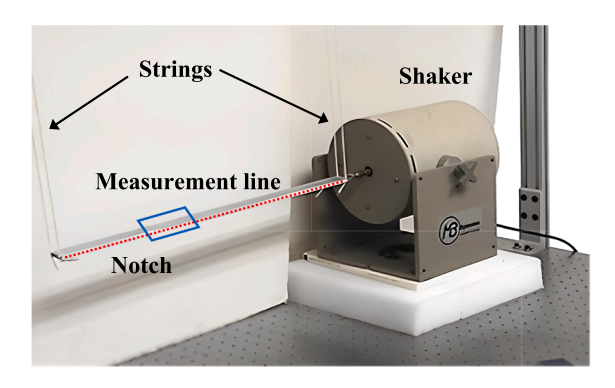
struggles to fit discontinuities induced by large-sized damage. Conversely, local fitting excels in characterizing such discontinuities by leveraging its inherent localization property. Specifically, damage-induced peaks in $\delta_{\rm I}[x]$ and $\delta_{\rm II}[x]$ at damage locations may be obscured by global fitting, while local fitting perfectly captures these peaks at damage edges. Therefore, when it comes to detecting damage in bars using longitudinal ODSs, local fitting demonstrates a superiority to global fitting in adapting to varying damage sizes.

4. Experimental validation

The proposed schemes of local fitting are experimentally validated by detecting a two-sided notch in a bar, whose longitudinal ODSs are measured through 3D laser scanning using a 3D-SLV.

4.1. Experimental specimen and setup

The experimental specimen, an aluminum bar with a two-sided notch, is illustrated in Fig. 10, whose Young's modulus, density, and dimensions are listed in Table 1. Through symmetrical milling, 1.25 mm in thickness is removed from both the top and bottom surfaces of the specimen through its width, creating a notch of 55 mm in length. The bar is suspended by four flexible strings that are glued to its four corners of the upper surface. For simplicity and repeatability, free boundary conditions are considered in this study. The bar is excited by an electromagnetic shaker (MB Dynamics Modal 50A), which is attached to the end of the bar farther away from the notch, as shown in Fig. 10(a). The measurement line is situated on a lateral side of the bar along its length, marked by dots in Fig. 10(a) representing the laser spot moving along the bar length. The measurement line spans 450 mm, starting 2 mm



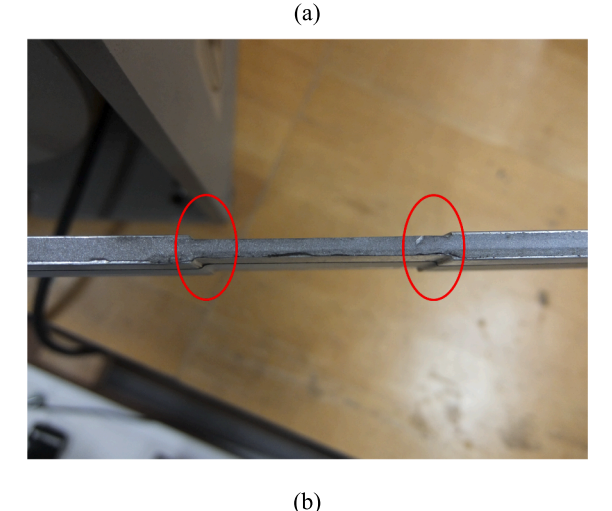


Fig. 10. (a) Aluminum bar with a two-sided notch and (b) the zoomed-in view of the notch.

Table 1Material and geometrical parameters of the experimental specimen.

Material parameters		Geometrical parameters		
Young's modulus	Density	Length	Width	Thickness
70.5 GPa	2680 kg/m ³	475 mm	25.4 mm	6.35 mm

away from the end of the bar without the shaker attached to it. The notch is positioned 145 through 200 mm away from the starting point of the measurement line, corresponding to the dimensionless coordinate $\zeta=0.322$ through 0.444. A zoomed-in view of the notch is presented in Fig. 10(b) to display the notch, whose edges are circled by two red ellipses.

The theoretical undamped fundamental longitudinal natural frequency of the bar is 4968.6 Hz. However, due to the limitation of the shaker used in this study, with a maximum excitation frequency of only 5000 Hz, the precise measurement of the exact fundamental longitudinal natural frequency of the bar is challenging. To address this limitation, the excitation frequency of the shaker is selected as 4900 Hz, which is close to the actual fundamental longitudinal natural frequency of the bar. The 3D-SLV (Polytec PSV-500-3D) is shown in Fig. 11, which measures steady-state velocity responses of the bar at 255 uniformly distributed measurement points along the measurement line. The longitudinal ODS at 4900 Hz is extracted using the LMS Test.Lab 9b's animation module by analyzing the averaged cross-power spectra of velocities at the measurement points.

4.2. Experimental results

As described in Section 2.1, the 3D components of steady-state velocities ν_1 , ν_2 , and ν_3 at each measurement point of the bar are measured by the 3D-SLV. After the geometrical transformation, the longitudinal velocity v_r and transverse velocities v_v and v_z are obtained using v_1 , v_2 , and v_3 . The time histories of v_x at all measurement points aligned in a line along the bar length are transformed to the frequency domain as \hat{v}_x by the fast Fourier transform, constituting a spacefrequency matrix. This matrix enables the formation of the ODS at the excitation frequency. It is important to note that the measured ODS consists of real and imaginary parts due to damping. In this study, the real part of the measured ODS in Fig. 12 is used for damage detection as it has a larger magnitude, resulting in a higher SNR. The measured ODS is denoised by Eqs. (8) and (9) at a satisfying scale of 35 determined after trials, which yields the corresponding MODS $U_s^M[x]$, as shown in a solid line in Fig. 13. By applying type-I local fitting to the measured MODS by Eq. (11), a locally fitted MODS $U_s^{F,L}[x]$ is obtained and also shown in a dotted line in Fig. 13. It can be observed from Fig. 13 that the curves $U_s^M[x]$ and $U_s^{F,L}[x]$ almost completely overlap. Note that in Figs. 12 and 13, locations of the damage edges are marked by two red dashed lines.

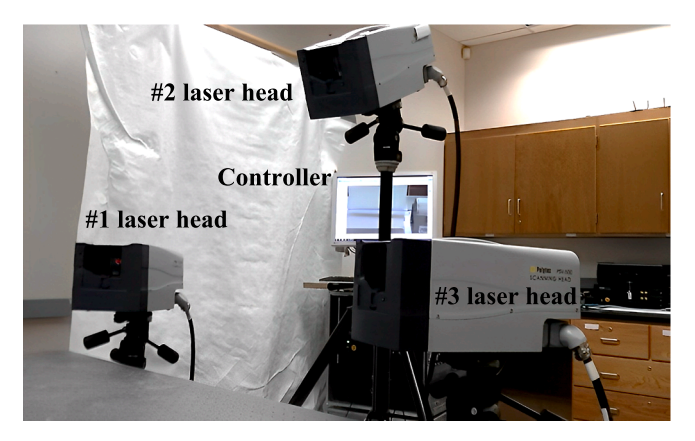


Fig. 11. 3D-SLV with three laser heads and its controller.

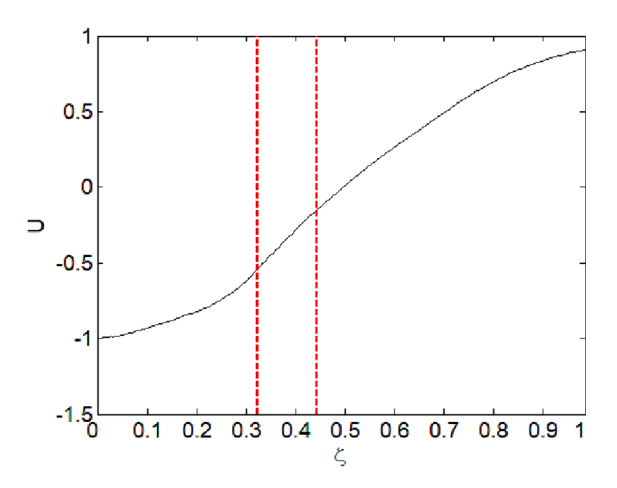


Fig. 12. Real part of the ODS measured by the 3D-SLV.

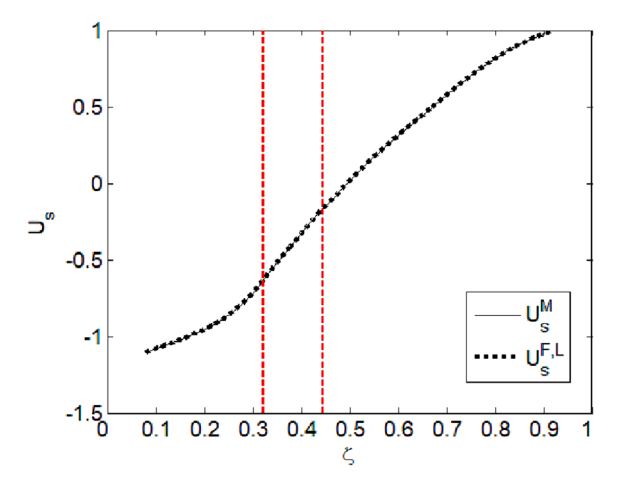


Fig. 13. MODS and the locally fitted MODS.

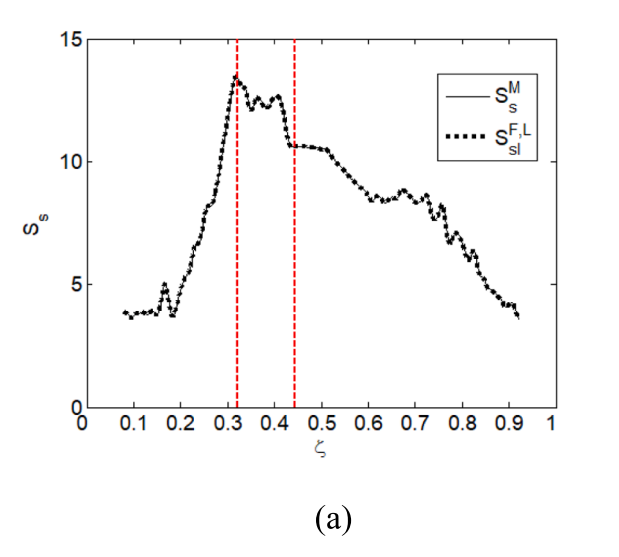
By applying type-I and type-II local fitting schemes, the corresponding MSODSs $S_{\rm sl}^{F,L}[x]$ and $S_{\rm sll}^{F,L}[x]$ are obtained, as shown in Fig. 14(a) and (b), respectively. Note that in Fig. 14, locations of the damage edges are marked by two red dashed lines. Accordingly, the type-I and type-II DIs ($DI_{\rm I}[x]$ and $DI_{\rm II}[x]$) are obtained by Eqs. (12) and (14), as shown in Fig. 15(a) and (b), respectively. As can be seen from the type-I DI in

Fig. 15(a), two peaks clearly indicate the presence of damage and its location that spans from about $\zeta=0.32$ through 0.45. However, some fake peaks appear at intact locations of the bar. In contrast, such influence of fake peaks becomes less pronounced in the type-II DI (see Fig. 15 (b)). Two peaks in $DI_{\rm II}[x]$ sharply rise to evidently pinpoint the notch that spans from about $\zeta=0.32$ through 0.45. The two red dashed lines in Fig. 15 at $\zeta=0.322$ and $\zeta=0.444$ that correspond to the actual locations of the damage edges validate that the notch is accurately localized. However, it is noticed that three fake peaks with subtle amplitudes still can be found in $DI_{\rm II}[x]$. To deal with this problem, more than one ODS associated with different excitation frequencies should be comprehensively considered in some future research.

5. Conclusions

In this study, two schemes (type-I and type-II) of local fitting are proposed for damage detection of bars. The analytical solutions to longitudinal ODSs of bars with local damage are employed to verify the capability of the two local fitting schemes. Additionally, the superiority of local fitting to global fitting in self-adaption to damage sizes is demonstrated through case comparison. An experiment involving the measurement of longitudinal ODSs of a bar is conducted using 3D laser scanning, and the proposed schemes are experimentally validated by detecting a two-sided notch in the bar. The theoretical and experimental results reveal that damage can be accurately pinpointed by locating its two edges. Some conclusions are as follows.

- (1) As noise components are inevitably involved in measured ODSs and can be amplified by differentiation operation, actual damage-induced discontinuities in SODSs can be masked by intense noise interference. To solve this problem, the multiscale analysis is introduced into ODSs: measured longitudinal ODSs in this study are inspected in a "region-by-region" manner instead of the conventional "point-by-point" manner. By gradually increasing scale parameters, noise components in ODSs can be eliminated while damage-induced discontinuities can be retained.
- (2) In the first scheme, type-I local fitting is proposed to fit measured MODSs through local cubic interpolation, allowing for reconstruction of locally fitted MODSs. By taking derivatives of MODSs, both measured and locally fitted MSODSs can be obtained, relying on the difference of which the type-I DI is established. Peaks that sharply arise in the type-I DI can evidently indicate locations of the damage edges.



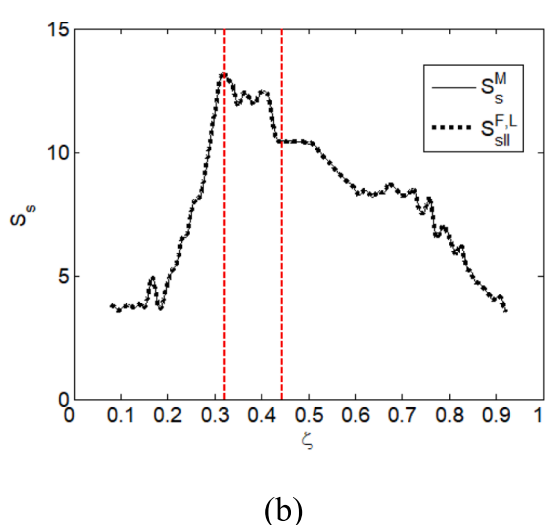
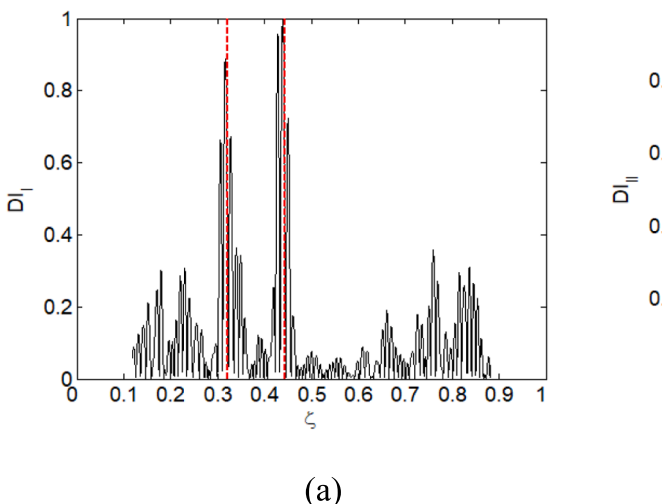
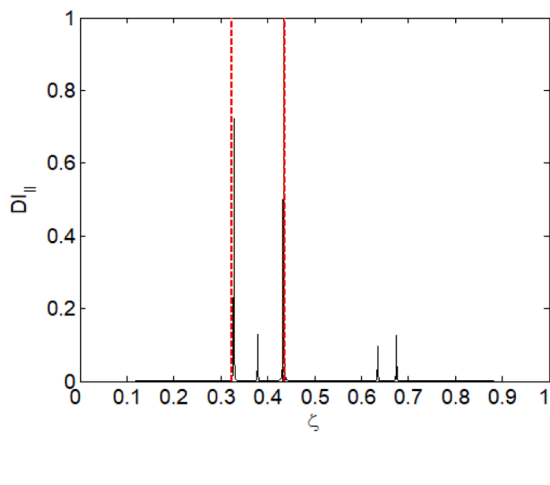


Fig. 14. Measured MSODSs and locally fitted MSODSs using (a) type-I and (b) type-II local fitting schemes.





(b)

Fig. 15. (a) Type-I and (b) type-II DIs.

- (3) In the second scheme, type-II local fitting is proposed to fit measured MSODSs through local cubic interpolation, enabling reconstruction of locally fitted MSODSs. The type-II DI is established relying on the difference between measured and locally fitted MSODSs. Compared to the type-I DI, the type-II DI demonstrates almost the same capability of indicating the presence of damage and locating damage edges.
- (4) In cases of damage detection of bars using longitudinal ODSs, local fitting exhibits a superiority to global fitting in self-adaption to damage sizes. Discontinuities induced by large-sized damage cannot be perfectly fitted by global fitting. In contrast, such discontinuities can be characterized by local fitting due to its localization property.

CRediT authorship contribution statement

Wei Xu: Conceptualization, Methodology, Software, Validation, Writing – original draft, Writing – review & editing. Ruiqi Li: Software. Weidong Zhu: Conceptualization, Formal analysis, Funding acquisition, Methodology, Validation, Writing – review & editing.

Declaration of competing interest

The authors declare that they have no known competing financial interests or personal relationships that could have appeared to influence the work reported in this paper.

Data availability

Data will be made available on request.

Acknowledgements

Weidong Zhu is grateful for the support from the National Science Foundation through Grant No. CMMI-1763024. The authors would like to thank Scott Smith in the Department of Mechanical Engineering at the University of Maryland, Baltimore County for the help on the experimental work.

References

[1] W. Xu, W. Zhu, S. Smith, M. Cao, Structural damage detection using slopes of longitudinal vibration shapes, J. Vib. Acoust. 138 (3) (2016) 034501.

- [2] W. Xu, W. Zhu, Y. Xu, M. Cao, A comparative study on structural damage detection using derivatives of laser-measured flexural and longitudinal vibration shapes, J. Nondestr. Eval. 39 (2020) 59.
- [3] W. Xu, W. Zhu, Z. Su, M. Cao, H. Xu, A novel structural damage identification approach using damage-induced perturbation in longitudinal vibration, J. Sound Vib. 496 (2021) 115932.
- [4] A. Pandey, M. Biswas, M. Samman, Damage detection from changes in curvature mode shapes, J. Sound Vib. 145 (1991) 321–332.
- [5] E. Sazonov, P. Klinkhachorn, Optimal spatial sampling interval for damage detection by curvature or strain energy mode shapes, J. Sound Vib. 285 (2005) 783–801.
- [6] P. Qiao, W. Lestari, M.G. Shah, J. Wang, Dynamics-based damage detection of composite laminated beams using contact and noncontact measurement systems, J. Compos. Mater. 41 (2007) 1217–1252.
- [7] M. Cao, P. Qiao, Novel laplacian scheme and multiresolution modal curvatures for structural damage identification, Mech. Syst. Sig. Process. 23 (2009) 1223–1242.
- [8] M. Yoon, D. Heider, J. Gillespie Jr., C. Ratcliffe, R. Crane, Local damage detection with the global fitting method using mode shape data in notched beams, J. Nondestr. Eval. 28 (2009) 63–74.
- [9] M. Yoon, D. Heider, J. Gillespie Jr., C. Ratcliffe, R. Crane, Local damage detection with the global fitting method using operating deflection shape data, J. Nondestr. Eval. 29 (2010) 25–37.
- [10] J. Kim, E. Lee, S. Rahmatalla, H. Eun, Non-baseline damage detection based on the deviation of displacement mode shape data, J. Nondestr. Eval. 32 (2013) 14–24.
- [11] M. Cao, W. Xu, W. Ostachowicz, Z. Su, Damage identification for beams in noisy conditions based on Teager energy operator-wavelet transform modal curvature, J. Sound Vib. 333 (2014) 1543–1553.
- [12] Y. Xu, W. Zhu, J. Liu, Y. Shao, Identification of embedded horizontal cracks in beams using measured mode shapes, J. Sound Vib. 333 (2014) 6273–6294.
- [13] S. Cao, H. Ouyang, Robust structural damage detection and localization based on joint approximate diagonalization technique in frequency domain, Smart Mater. Struct. 26 (2017) 015005.
- [14] Z. Yang, M. Radzienski, P. Kudela, W. Ostachowicz, Fourier spectral-based modal curvature analysis and its application to damage detection in beams, Mech. Syst. Sig. Process. 84 (2017) 763–781.
- [15] K. Liew, Q. Wang, Application of wavelet theory for crack identification in structures, J. Eng. Mech. 124 (1998) 152–157.
- [16] Q. Wang, X. Deng, Damage detection with spatial wavelets, Int. J. Solids Struct. 36 (1999) 3443–3468.
- [17] M. Rucka, K. Wilde, Application of continuous wavelet transform in vibration based damage detection method for beams and plates, J. Sound Vib. 297 (2006) 536–550.
- [18] H. Kim, H. Melhem, Damage detection of structures by wavelet analysis, Eng. Struct. 26 (2004) 347–362.
- [19] W. Xu, M. Cao, K. Ding, M. Radzieński, W. Ostachowicz, Crack identification in CFRP laminated beams using multi-resolution modal Teager-Kaiser energy under noisy environments, Materials. 10 (6) (2017) 656.
- [20] H. Xu, L. Cheng, Z. Su, J.-L. Guyader, Identification of structural damage based on locally perturbed dynamic equilibrium with an application to beam component, J. Sound Vib. 330 (24) (2011) 5963–5981.
- [21] M. Cao, L. Cheng, Z. Su, H. Xu, A multi-scale pseudo-force model in wavelet domain for identification of damage in structural components, Mech. Syst. Sig. Process. 28 (2012) 638–659.
- [22] M. Cao, Z. Su, L. Cheng, H. Xu, A multi-scale pseudo-force model for characterization of damage in beam components with unknown material and structural parameters, J. Sound Vib. 332 (21) (2013) 5566–5583.
- [23] H. Xu, Z. Su, L. Cheng, J. Guyader, P. Hamelin, Reconstructing interfacial force distribution for identification of multi-debonding in steel-reinforced concrete

- structures using noncontact laser vibrometry, Struct. Health Monit.-An Int. J. 12 (2013) 507–521.
- [24] H. Xu, L. Cheng, Z. Su, Suppressing influence of measurement noise on vibration-based damage detection involving higher-order derivatives, Adv. Struct. Eng. 16 (1) (2013) 233–244.
- [25] H. Xu, Z. Su, L. Cheng, J.-L. Guyader, A "pseudo-excitation" approach for structural damage identification: from "strong" to "weak" modality, J. Sound Vib. 337 (2015) 181–198.
- [26] C. Zhang, H. Ji, J. Qiu, L. Cheng, W. Yao, Y. Wu, A local specific stiffness identification method based on a multi-scale "weak" formulation, Mech. Syst. Sig. Process. 140 (2020) 106650.
- [27] A. Deng, M. Cao, Q. Lu, W. Xu, Identification of multiple cracks in composite laminated beams using perturbation to dynamic equilibrium, Sensors 21 (18) (2021) 6171.
- [28] W. Weaver Jr, S. Timoshenko, D. Young, Vibration problems in engineering, John Wiley & Sons, 1990.
- [29] Ł. Pieczonka, Ł. Ambroziński, W. Staszewski, D. Barnoncel, P. Pérès, Damage detection in composite panels based on mode-converted lamb waves sensed using 3D laser scanning vibrometer, Opt. Lasers Eng. 99 (2017) 80–87.
- [30] A. Buades, B. Coll, J.M. Morel, A review of image denoising algorithms, with a new one, Multiscale Model. Simul. 4 (2) (2005) 490–530.
- [31] S. Mallat, A wavelet tour of signal processing, Academic Press, 2008.